nature communications

Article

https://doi.org/10.1038/s41467-026-75394-x

Modulating the interfacial solvation structure to promote hydroxyl migration for alkaline hydrogen oxidation

Received: 2 February 2026

Accepted: 29 June 2026

Published online: 10 July 2026

Check for updates

Chenggong Niu[1], Yulin Zhao[2,9], Yuchen Lei[2], Linyu Chen[1], Zuyang Luo[1], Heyang Liu[1], Tingting Tang[1], Xiaofeng Shi[3] ✉, Lianhai Zu[4], Wei Zhao[2], Xiulin Yang[1] ✉, Rui Cao[5], Jieshan Qiu[6], Yongfa Zhu[7] ✉ & Bin Wu[8] ✉

Alkaline hydrogen oxidation reaction (HOR) kinetics are fundamentally governed by electrode-electrolyte interfacial water structure and hydrogen-bond (H-bond) networks, yet their dynamic regulatory mechanism remains elusive. Here we show that precise modulation of the P coordination environment of Ir-based catalysts effectively enhances alkaline HOR catalytic performance. A series of Ir-based model catalysts with tunable P-coordination numbers are synthesized on nitrogen-doped carbon (NC) (IrP_2-Ir_2P@NC, IrP_2@NC, Ir@NC). The optimal Ir-P coordination (5.1 ± 0.7) induces controlled partial dissolution of Ir cations, a dynamic phenomenon rarely exploited in alkaline HOR catalysis. This effect reconstructs the interfacial H-bond network via enriched gap-H_2O and strengthened network connectivity, while optimizing hydrogen and hydroxyl adsorption to accelerate the Volmer step. The optimized IrP_2-Ir_2P@NC delivers a mass activity of 1.72 mA μg^{-1} and a prominent alkaline exchange membrane fuel cell (AEMFC) peak power density of 1.59 W cm^{-2}. Ab initio molecular dynamics simulations confirm modified solvation structure elevates interfacial H-bond density, thereby elucidating the previously unresolved mechanism by which cation dissolution dynamically templates the H-bond network for enhanced HOR performance.

Electrochemical energy conversion presents potential solutions to global challenges such as environmental pollution and the energy crisis[1–3]. Anion exchange membrane fuel cells (AEMFCs) stand out due to their ability to directly convert hydrogen fuel-an environmentally friendly, zero-carbon energy source with high energy density-into electrical energy under alkaline conditions[2,4–7]. Unfortunately, the transition from an acidic to an alkaline medium typically results in a two orders magnitude decrease in the HOR kinetics, which hinders its widespread commercial application[8,9]. Consequently, substantial efforts are devoted to exploring efficient catalysts for alkaline HOR. Advancements in-situ characterization have enabled the observation of adsorbed hydroxyl (OH_{ad}) during the HOR reaction process[10]. OH_{ad}

[1]Guangxi Key Laboratory of Low Carbon Energy Materials, School of Chemistry and Pharmaceutical Sciences, Guangxi Normal University, Guilin, China. [2]Institute for Advanced Study, Shenzhen University, Shenzhen, China. [3]School of Environment and Safety Engineering, North University of China, Taiyuan, China. [4]Shanghai Advanced Research Institute, Chinese Academy of Sciences, Shanghai, China. [5]Key Laboratory of Applied Surface and Colloid Chemistry, Ministry of Education, School of Chemistry and Chemical Engineering, Shaanxi Normal University, Xi'an, China. [6]State Key Laboratory of Organic-Inorganic Composites, Beijing University of Chemical Technology, Beijing, China. [7]Department of Chemistry, Tsinghua University, Beijing, China. [8]School of Materials Science and Engineering, Nanyang Technological University, Singapore, Singapore. [9]Present address: Key Laboratory of Biomass Chemical Engineering of Ministry of Education, College of Chemical and Biological Engineering, Zhejiang University, Hangzhou, China.
✉e-mail: xiaofeng_shi1987@163.com; xlyang@gxnu.edu.cn; zhuyf@tsinghua.edu.cn; bin.wu@ntu.edu.sg

species can be used as descriptors for the HOR reaction process[11–14]. However, the interaction between key intermediate hydroxyl groups and interfacial water is often overlooked.

Currently, the Volmer step involving hydroxyl adsorption (OH^- - $e^- \rightarrow OH_{ad}$) and the subsequent water formation ($OH_{ad} + H_{ad} \rightarrow H_2O$) are generally considered as the rate-determining step (RDS)[11,15,16]. Recent investigations indicate that adsorbed hydroxyl groups are critical determinants of the kinetics of alkaline HOR[17]. From a molecular perspective, there exist complex interactions between the OH_{ad} groups adsorbed over the electrode surface and the adjacent interfacial water molecules[17–19]. These interactions are exhibited not only by intermolecular electrostatic gravitational forces and van der Waals forces, but more importantly, the interfacial water molecules can regulate the hydroxyl groups through the formation of hydrogen bond networks[17,20–22]. Currently, tuning the electronic structure through alloying, doping, and defect engineering is employed to facilitate the formation of H-OH bonds and promote HOR kinetics[1,2,23–26]. However, there are still obvious limitations in the current research on the alkaline HOR field. Initially, most studies focus on optimizing the binding energy of OH_{ad} by regulating the electronic structure of the electrode, while neglecting the quantitative analysis of the dynamic interactions between adsorbed intermediates (OH_{ad}, H_{ad}) and interfacial water molecules[27]. Second, the influence of dissolved metals on interfacial water and hydrogen bond networks has been overlooked[28]. Against this background, exploring the interactions between adsorbed intermediates and interfacial water molecules, along with the influence of metal cations on interfacial water and hydrogen bond networks, provides a promising approach to advance high-performance HOR catalysts.

In this work, a series of catalysts (including IrP_2-Ir_2P@NC, IrP_2@NC and Ir@NC) were designed. Initially, the adsorption behaviors of different catalysts were investigated via DFT simulations, and it was found that IrP_2-Ir_2P@NC exhibited the optimal adsorption of *H and *OH adsorptions, which reduced the energy barrier for water formation and accelerated the Volmer step. The Ir-P component of these catalysts was characterized by being only affected by the P coordination number, which served to investigate the effect of different P coordination numbers on the alkaline HOR of these Ir-P compounds. Under H_2-O_2 atmosphere, IrP_2-Ir_2P@NC was employed as the anode of the AEMFC, delivering a peak power density of 1.59 W cm^{-2}. Based on Coulomb's law, quasi-in-situ XPS and quasi-in situ absorption spectroscopy, it was concluded that an appropriate amount of P coordination weakened the strength of Ir-P bonds, leading to partial dissolution of Ir and thus achieving a solvation enhancement effect. Combined with in-situ characterizations, this solvation enhancement effect was found to help increase the content of gap-H_2O and strengthen the connectivity of the hydrogen bond network, which was beneficial for adjusting the point of zero charge (PZC) and promoting hydroxyl adsorption. AIMD further confirmed that the solvation enhancement effect from partial Ir dissolution strengthened the hydrogen bond network connectivity, thereby effectively improving the catalytic activity of alkaline HOR.

Results

DFT theoretical predictions

Based on our proposed concept, a series of catalytic models with different P coordination configurations (IrP_2-Ir_2P@NC, IrP_2@NC, Ir@NC) were designed (Supplementary Fig. 1 and Supplementary Data 1). The corresponding HOR processes were systematically investigated via density functional theory (DFT) simulations. The Crystal orbital hamiltonian population (COHP) values of different catalysts were calculated separately using the OH adsorption models and CO adsorption models (Supplementary Figs. 2, 3). The results demonstrated that the introduction of an appropriate amount of P effectively improved the OH adsorption capacity and CO poisoning resistance of the catalyst (Fig. 1a–c and Supplementary Figs. 4, 5 and 6). The differential charge analysis via Supplementary Fig. 7 indicated that the electron clouds of IrP_2@NC and Ir@NC were mainly concentrated at the bottom, whereas the electron cloud of IrP_2-Ir_2P@NC was concentrated not only at the crystal interface but also at the bottom, indicating that an appropriate amount of P coordination was helpful for enhancing the intense electronic interaction between P and Ir. Compared with IrP_2@NC and Ir@NC, IrP_2-Ir_2P@NC exhibited a higher occupancy of total density of states (DOS) in proximity to the Fermi level. This indicates that IrP_2-Ir_2P@NC has more electron states accessible for electron occupation and mobility, thereby enhancing the electronic conductivity (Fig. 1d). In Fig. 1e, the *d*-band centers of IrP_2-Ir_2P@NC, IrP_2@NC and Ir@NC were −2.12 eV, −2.23 eV, and −1.93 eV, respectively. This result indicated that appropriate P coordination was beneficial for enhancing hydroxyl adsorption[29].

Furthermore, the theoretical model of CO-metal bonding revealed the mechanism of electronic structure interaction (Supplementary Fig. 8)[30,31]. Partial electrons from the 5σ orbital of the CO molecule transferred to the metal *d* orbitals, while electrons from the metal *d* orbitals back-donated to the 2π* antibonding orbital of CO. Thus, the interaction could be reflected by tuning the *d*-band center and enhancing the OH adsorption capability. The *d*-band center of IrP_2-Ir_2P@NC lay between those of IrP_2@NC and Ir@NC. This shift originated from charge transfer induced by tuning the number of P coordinations, which synergistically optimized the adsorption strengths of H and OH. Accordingly, the back-donation of electrons from Ir *d* orbitals to the 2π* antibonding orbital of CO was suppressed, endowing IrP_2-Ir_2P@NC with moderate resistance toward CO poisoning[32]. The binding affinities of essential intermediates were calculated. Supplementary Figs. 2, 9 display the adsorption sites of IrP_2-Ir_2P@NC, IrP_2@NC and Ir@NC. As shown in Supplementary Fig. 10, IrP_2-Ir_2P@NC demonstrated the lowest hydrogen binding energy of −0.81 eV, in contrast to IrP_2@NC (−1.28 eV) and Ir@NC (−1.19 eV), indicating that the HOR process was favorable. Additionally, as derived from Fig. 1f, IrP_2-Ir_2P@NC exhibited the highest hydroxyl binding energy of −1.73 eV. This was consistent with the results obtained from COHP. Therefore, the above results indicated that appropriate P coordination enabled IrP_2-Ir_2P@NC to achieve optimal HBE and OHBE. To further explore the regulatory effect of applied voltage on the electronic structure and adsorption behavior of catalysts, we calculated and analyzed the DOS and OHBE of different catalysts at a potential of 0.1 V, as displayed in Supplementary Figs. 11 and 12. As the applied voltage increased, the charge quantity of the catalyst system gradually decreased, the number of electrons in the bonding state was reduced, and the overall energy band structure shifted downward. Meanwhile, it was observed that the increase in voltage significantly strengthened the hydroxyl adsorption strength of the catalysts, following the order of IrP_2-Ir_2P@NC > Ir@NC > IrP_2@NC. Overall, appropriate P coordination effectively modulated the electronic structure of the catalysts and further enhanced their hydroxyl adsorption capability. Additionally, the adsorption energies of CO* on different catalysts were calculated, and the adsorption sites are shown in Supplementary Fig. 3. The CO* adsorption energies followed the order: IrP_2-Ir_2P@NC (−1.29 eV) < Ir@NC (−1.49 eV) < IrP_2@NC (−1.53 eV), indicating that appropriate P coordination helped tune the electronic structure of Ir, thereby enhancing its CO poisoning resistance (Fig. 1g). This was consistent with the results obtained from the aforementioned COHP and *d*-band center analyses. Additionally, the energy profiles of IrP_2-Ir_2P@NC, IrP_2@NC and Ir@NC during the alkaline HOR process were calculated, and the theoretical models involved. As expected, IrP_2-Ir_2P@NC exhibited the lowest water formation energy barrier of 1.32 eV, compared to IrP_2@NC (1.69 eV) and Ir@NC (1.58 eV), indicating improved HOR kinetics (Fig. 1h). Notably, DFT adopted simplified computational approximations and could not fully replicate the complex environments of real electrodes, which imposed inherent restrictions on the quantitative interpretation of experimental observations.

https://doi.org/10.1038/s41467-026-75394-x

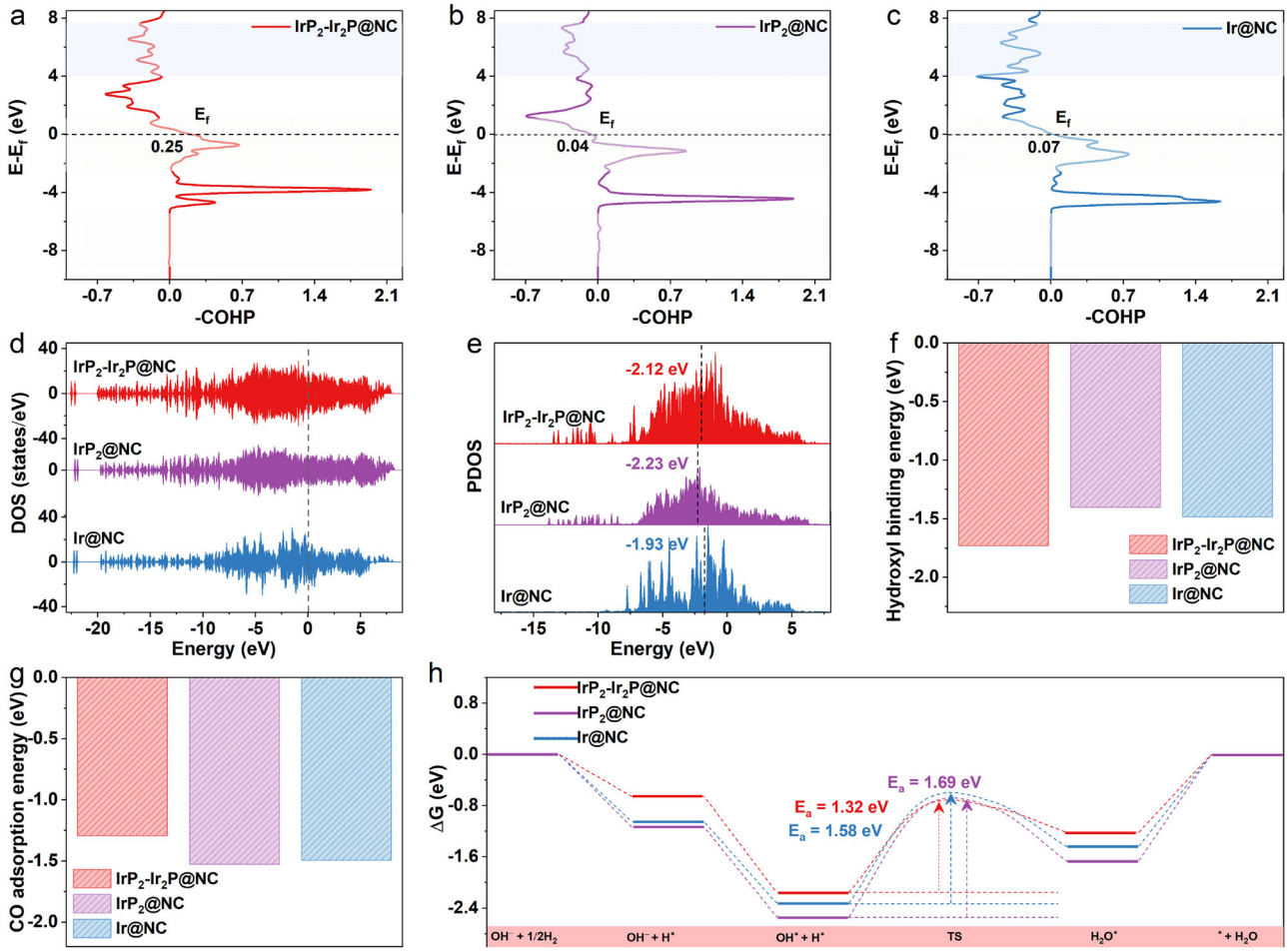

Fig. 1 | Theoretical calculation results. a–c Calculated COHP of IrP_2-Ir_2P@NC, IrP_2@NC and Ir@NC. **d** The density of state (DOS) plots. **e** PDOS and Ir d-band center values, **f** Calculated OHBEs for IrP_2-Ir_2P@NC, IrP_2@NC and Ir@NC. **g** CO adsorption energies, **h** Gibbs free energy profiles of basic HOR on the surfaces. Source data for Fig. 1 are provided as a Source Data file.

Morphological and structural characterizations

Guided by the DFT simulations. IrP_2-Ir_2P@NC catalytic model was rationally constructed (Fig. 2a). Initially, $Zn(NO_3)_2{\cdot}6H_2O$ and 2-methylimidazole were individually solubilized in methanol. After mixing, ZIF-8 crystals were synthesized by coordination following the mixing process. Subsequently, ZIF-8 was pyrolyzed to convert into nitrogen-doped carbon (NC) with a porous structure (Supplementary Fig. 13). Then, under ultrasonic conditions, Ir species and triphenylphosphine were added to the mixed solution containing NC. Finally, the target catalyst (denoted as IrP_2-Ir_2P@NC) was synthesized via pyrolysis. Initially, the successful preparation of Ir-based phosphides and metallic Ir were confirmed by X-ray diffraction (XRD) patterns. They were consistent with Ir (JCPDS: 87-0715), IrP_2 (JCPDS: 89-3985), and Ir_2P (JCPDS: 77-0299), respectively (Fig. 2b and Supplementary Fig. 14). Raman spectroscopy was used to evaluate the catalysts structural defects. Two bands within the observed range, D (1319 cm^{-1}) and G (1597 cm^{-1}), corresponded to disordered sp^3 and sp^2 hybridized carbon atoms, respectively[33]. Compared with IrP_2@NC and Ir@NC, IrP_2-Ir_2P@NC demonstrated a higher intensity ratio (I_D/I_G), demonstrating that the appropriate doping of P loading promoted the generation of more carbon defects (Supplementary Fig. 15)[34]. The N_2 adsorption-desorption isotherm showed that IrP_2-Ir_2P@NC (719.29 m^2 g^{-1}) exhibited a larger specific surface area than IrP_2@NC (446.35 m^2 g^{-1}) and Ir@NC (579.66 m^2 g^{-1}), which helped expose more active sites and accelerate reaction kinetics (Supplementary Figs. 16, 17 and 18)[35].

To further examine the atomic-level characteristics of the catalyst, field-emission scanning electron microscopy (SEM) and transmission electron microscopy (TEM) were used. The NC structure was observed by SEM to exhibit a dodecahedral morphology (Supplementary Fig. 19). TEM was used to observe the morphology of the materials. Loading the catalyst onto NC resulted in the generation of particles. As demonstrated in Supplementary Fig. 20, the average particle diameter of IrP_2-Ir_2P@NC was 11.74 nm. To further investigate the local atomic arrangements, we utilized aberration-corrected high-angle annular dark-field scanning transmission electron microscopy (HAADF-STEM) and TEM. AC AADF-STEM was employed to observe lattice fringes with spacings of 0.225 and 0.312 nm corresponding to the (−212) plane of IrP_2 and the (111) plane of Ir_2P, respectively (Fig. 2c–e). Moreover, As illustrated in Fig. 2f, g and Supplementary Fig. 21 illustrate that TEM analysis indicated lattice spacings of 0.233 and 0.199 nm, which are ascribed to the (−202) crystal plane of IrP_2 and the (−202) crystal plane of Ir_2P, respectively. Selected area electron diffraction (SAED) examination revealed diffraction patterns associated with IrP_2 (−102), IrP_2 (−312) and Ir_2P (220) (Fig. 2h). The results validated the effective synthesis of IrP_2-Ir_2P@NC. As depicted in Supplementary Figs. 22, 23 and 24, illustrate lattice fringes with interplanar lengths distances of 0.205 nm, 0.183 nm and 0.141 nm, which were consistent with the (220) plane of Ir_2P, (−113) plane of IrP_2 and the (220) plane of Ir, respectively. These experimental results were in accordance with the XRD data, providing another evidence for the successful synthesis of IrP_2 and Ir_2P. Additionally, the elemental mapping images verified the homogeneous distribution of C, N, P and Ir (Supplementary Figs. 25, 26).

https://doi.org/10.1038/s41467-026-75394-x

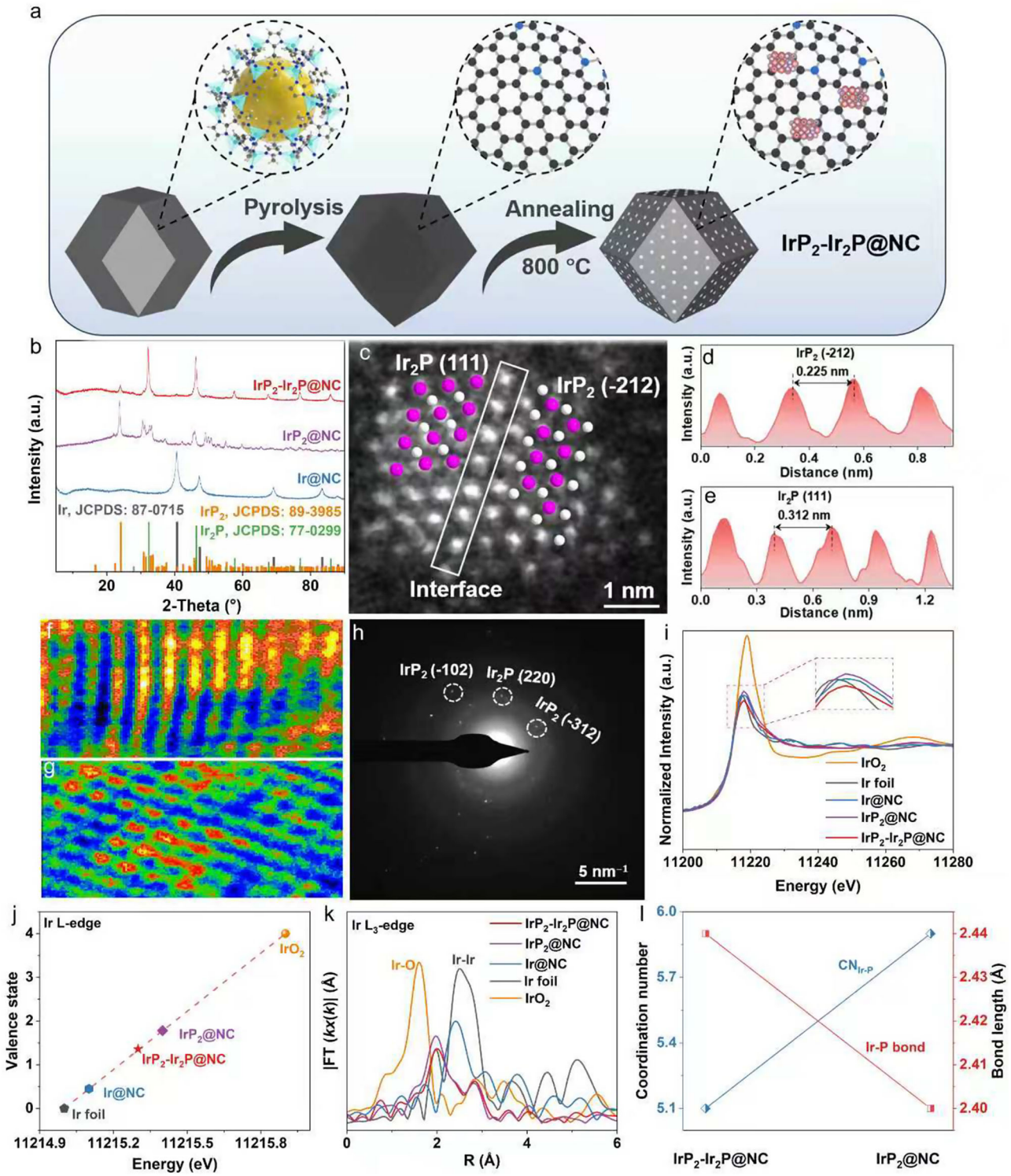

Fig. 2 | Synthesis and characterization of IrP_2-Ir_2P@NC. a Schematic illustration of the general synthetic process for IrP_2-Ir_2P@NC (black: C; blue: N; light red: Ir; light purple: P). **b** XRD patterns of IrP_2-Ir_2P@NC, IrP_2@NC, Ir@NC. **c** AC HAADF-STEM image of IrP_2-Ir_2P@NC (pink: Ir; white: P). **d**, **e** Intensity profiles of IrP_2-Ir_2P@NC acquired from (c). **f**, **g** IFFT images at different areas of IrP_2-Ir_2P@NC acquired from (Supplementary Fig. 21). **h** SAED pattern of IrP_2-Ir_2P@NC. **i** Ir L_3-edge XANES spectra of IrP_2-Ir_2P@NC, IrP_2@NC, Ir@NC, Ir foil and IrO_2. **j** Determination of Ir oxidation in IrP_2-Ir_2P@NC, IrP_2@NC and Ir@NC with reference samples of Ir foil and IrO_2 to ascertain the average oxidation state acquired from (i). **k** Corresponding Fourier transformed the EXAFS spectrum spectra of the IrP_2-Ir_2P@NC, IrP_2@NC, Ir@NC, Ir foil and IrO_2. **l** Ir-P coordination number and Ir-P bond length of IrP_2-Ir_2P@NC and IrP_2@NC IFFT images at different areas of IrP_2-Ir_2P@NC acquired from (Supplementary Table 1). Source data for Fig. 2 are provided as a Source Data file.

To qualitatively detect the presence of vacancies in the samples, electron paramagnetic resonance (EPR) measurements were performed. Supplementary Fig. 27 illustrated that IrP_2-Ir_2P@NC displayed a signal peak compared to IrP_2@NC and Ir@NC, signifying the existence of P vacancies[36]. Additionally, X-ray photoelectron spectroscopy (XPS) was used to analyze the surface composition and valence states. As illustrated in Supplementary Fig. 28, in the Ir 4*f* spectrum, the peaks at approximately 60.25 eV and 60.94 eV corresponded to the

Ir-P and Ir-Ir bonds, respectively[37,38]. Compared with other materials, the binding energy of Ir-P bonds in IrP_2-Ir_2P@NC was lower than that in IrP_2@NC but higher than that in Ir_2P@NC. This indicated that with increasing P coordination number, the charge of Ir decreased while its valence state increased slightly. Additionally, the Ir 4*f* spectrum of Ir@NC is shown in Supplementary Fig. 29.

To further explore the electronic states and coordination environments of metal species in IrP_2-Ir_2P@NC, IrP_2@NC and Ir@NC, synchrotron X-ray absorption spectroscopy (XAS) was employed. Normalized X-ray absorption near-edge spectroscopy (XANES) at the Ir L-edge was performed with Ir foil and IrO_2 as references (Fig. 2i). Based on the scaling relationship between absorption energy and Ir valence state, the average valence state of Ir in IrP_2-Ir_2P@NC was 1.33, lying between 1.76 in IrP_2@NC and 0.45 in Ir@NC. This indicated that the introduction of P promoted electron loss of Ir (Fig. 2j)[39,40]. Furthermore, Ir L-edge extended X-ray absorption fine structure (EXAFS) spectra were collected to analyze the local environment of Ir atoms (Fig. 2k). The EXAFS spectra of Ir@NC displayed a distinct peak at 2.42 Å, akin to that of Ir foil, which could be attributed to the Ir-Ir bond. With the introduction of P, IrP_2-Ir_2P@NC and IrP_2@NC exhibited peaks at 2.01 Å and 1.97 Å, respectively, which could be attributed to the Ir-P bond. Specifically, compared with IrP_2@NC, the Ir-P signal peak in IrP_2-Ir_2P@NC exhibited a minor positive shift, signifying a modest elongation of the Ir-P bond in IrP_2-Ir_2P@NC. Additional curve fitting was performed to determine the specific structural parameters around the Ir atoms (Supplementary Figs. 30, 31 and 32). The analysis revealed that the coordination number of Ir-P in IrP_2-Ir_2P@NC was 5.1, which was lower than that in IrP_2@NC (CN = 5.9) (Supplementary Table 1). The distinct coordination environments of IrP_2-Ir_2P@NC, IrP_2@NC and Ir@NC were further investigated, aligning with the aforementioned EXAFS results (Supplementary Figs. 33-37). Figure 2l demonstrated that the Ir-P bond length progressively diminished as the coordination number of P in the catalyst increased[41].

HOR performance in alkaline media and catalytic mechanism unraveling

The electrocatalytic performance of the prepared catalysts HOR was evaluated in H_2-saturated 0.1 M KOH using a rotating disk electrode (RDE) in a standard three-electrode system. We initially examined the influence of various reaction conditions on the catalytic performance of IrP_2-Ir_2P@NC. We determined that the catalytic performance of IrP_2-Ir_2P@NC reached a peaked at 800 °C with an Ir concentration of 10.26 wt.% (Supplementary Figs. 38, 39 and Table 2). Figure 3a and Supplementary Fig. 40 demonstrates that, IrP_2-Ir_2P@NC displayed markedly enhanced HOR activity. The measured activity followed the order Ir_2P@NC > Ir_2P@NC > Ir@NC > IrP_2@NC, further indicating that appropriate P coordination contributed to enhanced catalytic activity. In the N_2-saturated control experiment, the anodic current was confirmed to originate from the oxidation of H_2 (Supplementary Fig. 41)[42]. The HOR polarization curves of IrP_2-Ir_2P@NC were examined at different rotation speeds were studied. The current density increased as the rotation speed increased, signifying the mass transfer process of H_2 (Supplementary Fig. 42a)[43]. According to the Koutecky-Levich equation, the calculated slope of IrP_2-Ir_2P@NC was 5.56 $cm^2\ mA^{-1}\ s^{-1/2}$, which was closely consistent with the theoretical value of 4.87 $cm^2\ mA^{-1}\ s^{-1/2}$, indicating a two-electron transfer process (Supplementary Fig. 42b)[43]. The asymmetric behavior observed from the Tafel plot suggested that IrP_2-Ir_2P@NC aligned with the Heyrovsky-Volmer mechanism, with the Volmer step recognized as the RDS (Fig. 3b)[44]. Figure 3c summarized the j_k values of different catalysts. The j_k value of IrP_2-Ir_2P@NC was 31.56 mA cm^{-2}, exceeding those of IrP_2@NC (1.22 mA cm^{-2}), Ir@NC (3.24 mA cm^{-2}) and Pt/C (10.21 mA cm^{-2}). IrP_2-Ir_2P@NC demonstrated mass activity (1.72 mA μg^{-1}), surpassing the majority of documented HOR catalysts (Supplementary Fig. 43 and Supplementary Table 3, 4). Subsequently, an accelerated stability test was implemented by chronoamperometry in H_2-saturated 0.1 M KOH. Supplementary Fig. 44 demonstrated that IrP_2-Ir_2P@NC displayed a milder reduction in current density in comparison to IrP_2@NC, Ir@NC and Pt/C, underscoring the acceptable long-term stability of IrP_2-Ir_2P@NC. Furthermore, we analyzed the dissolution amount of metallic Ir combined with the stability trend, as shown in Supplementary Fig. 45. In the initial stage of the reaction, the activity of IrP_2-Ir_2P@NC increased continuously with the dissolution of metallic Ir. The catalytic activity reached its maximum when the Ir dissolution amount reached 6.26 ppb, and then began to decrease gradually. When the dissolution amount reached 19.22 ppb, the catalytic activity of IrP_2-Ir_2P@NC stabilized. To evaluate the CO tolerance of the catalyst, we performed relevant experiments under an atmosphere of H_2/1000 ppm CO. The results showed that the polarization curve of IrP_2-Ir_2P@NC almost overlapped with the initial curve. In contrast, the current density of Pt/C decreased sharply under the same CO concentration, indicating that IrP_2-Ir_2P@NC exhibited moderate resistance to CO poisoning[45] (Fig. 3d). Furthermore, to further evaluate the CO tolerance of the catalyst, we performed chronoamperometric response measurements. As shown in Supplementary Fig. 46, the current retention of IrP_2-Ir_2P@NC was significantly higher than that of commercial Pt/C, which further confirmed the moderate CO poisoning resistance of IrP_2-Ir_2P@NC.

To further assess the HOR catalytic activity of the catalyst, we examined it by probing the binding strength of OH. The adsorption behavior of OH_{ad} was analyzed by CO stripping[29]. Figure 3e illustrates, IrP_2-Ir_2P@NC (0.66 V) had a greater negative value than IrP_2@NC (0.82 V), Ir@NC (0.79 V), and Pt/C (0.71 V), signifying that IrP_2-Ir_2P@NC had relatively higher OH binding energy (OHBE), conforming to the reported HOR activity[46,47]. To investigate the practical application of IrP_2-Ir_2P@NC in fuel cells, we employed IrP_2-Ir_2P@NC as the anode catalyst and commercial Pt/C as the cathode catalyst for an anion exchange membrane fuel cell (AEMFC) (Fig. 3f). Notably, the AEMFC with IrP_2-Ir_2P@NC delivered peak power densities (PPD) of 1.59 W cm^{-2} and 1.27 W cm^{-2} under H_2-O_2 and H_2-Air atmospheres, respectively, and such performance was competitive against values from recently documented HOR catalysts (Fig. 3g, Supplementary Fig. 47 and Supplementary Table 5, 6). To further verify the practical durability of the catalyst, we performed a long-term AEMFC stability test under H_2/O_2 atmosphere at a voltage of 0.7 V. As shown in Supplementary Fig. 48, IrP_2-Ir_2P@NC operated continuously for 100 h and maintained high stability. In addition, ICP-MS analysis of the electrolyte after the long-term reaction showed that the Ir dissolution amount was approximately 104.3 ppb. This result further demonstrated that appropriate Ir dissolution contributed to long-term and efficient catalysis. To investigate the changes of the catalyst after the long-term stability test, we characterized the post-reaction sample. As displayed in Supplementary Figs. 49, 50 and 51, the structure and composition of the catalyst remained intact without obvious changes, further confirming the structural stability of the catalyst.

Effect of P coordination on Ir-P bond dynamic evolution and origin of HOR activity

The bond strength influenced the interaction between the catalyst and adsorbates, therefore altering the electrocatalytic performance. Coulomb's law ($F \propto Qq/r^2$) indicates that bond strength (F) was related to the atomic valence charges (Q, q) and bond length (r)[48]. Generally, bond length stretching and valence state decrease led to the weakening of bond strength. As shown in Fig. 4a, b, in contrast to IrP_2@NC, the Ir-P bonds in IrP_2-Ir_2P@NC underwent elongation and valence state decrease, resulting in diminished bond strength. Thus, we hypothesized that the Ir-P bonds would be partially dissolved during the electrochemical reaction, thereby enhancing the alkaline HOR activity. To further confirm our hypothesis, we investigated the changes in the content of Ir-P bonds during the reaction via quasi-in-situ XPS. The

https://doi.org/10.1038/s41467-026-75394-x

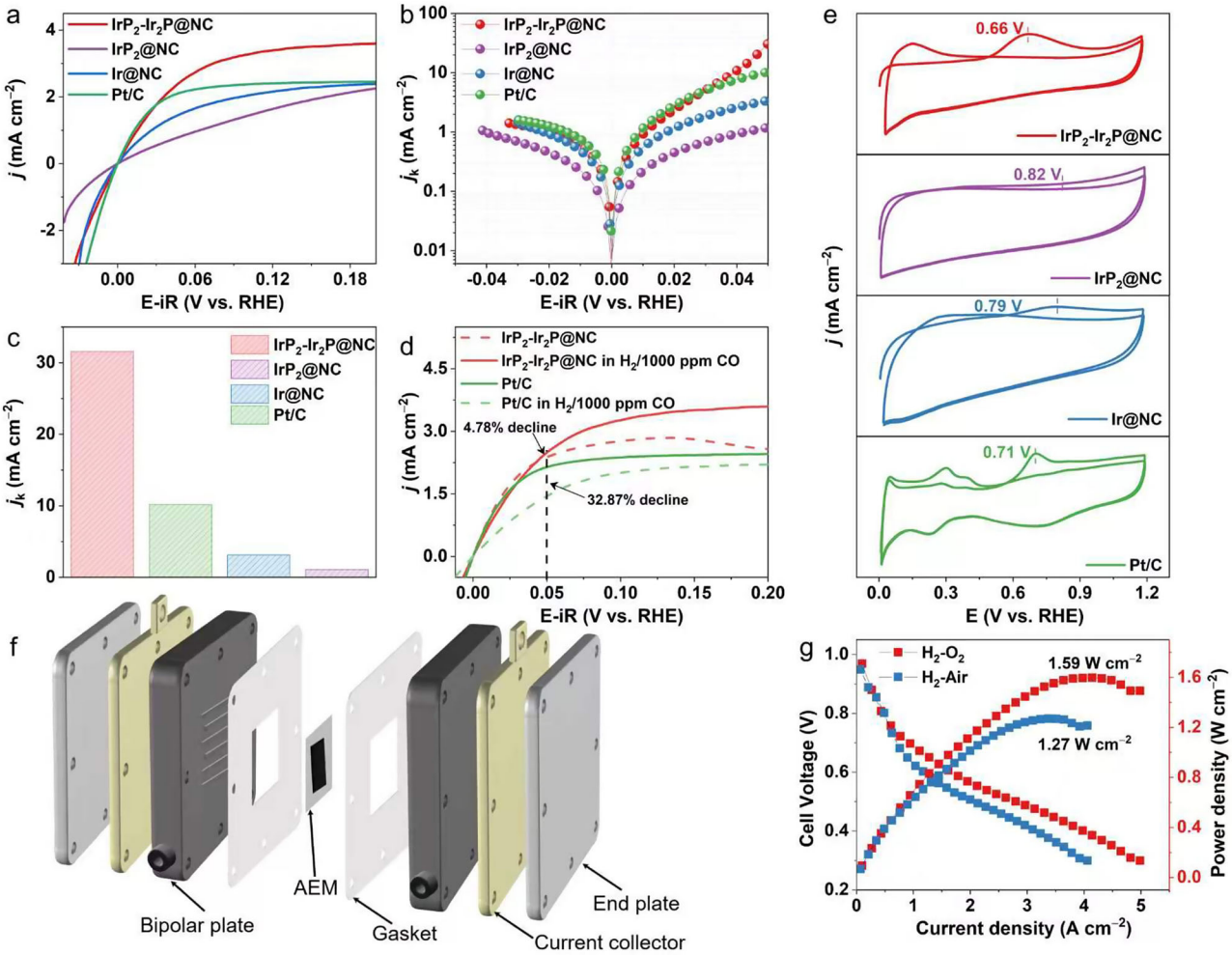

Fig. 3 | Electrocatalytic alkaline HOR performances. a Polarization curves for HOR over IrP_2-Ir_2P@NC, IrP_2@NC, Ir@NC and commercial Pt/C catalysts. Operation conditions: 0.1 M KOH electrolyte (pH = 12.9 ± 0.01), scan rate of 10 mV s^{-1}, Ir mass loading of 47.59 μg_{Ir} cm^{-2}, rotating speed of 1600 rpm, continuous H_2 flow rate of 25 sccm, working electrode: 5 mm-diameter GCE with geometric area of 0.196 cm^2, test temperature of 25 ± 2 °C. **b** Tafel plots. **c** Comparison of j_k for studied electrocatalysts acquired from (b). **d** HOR performance of IrP_2-Ir_2P@NC and Pt/C in pure H_2 and H_2/1000 ppm CO. **e** CO stripping curves of IrP_2-Ir_2P@NC, IrP_2@NC, Ir@NC and Pt/C. **f** Schematic illustration of the AEMFC. **g** Polarization and power density curves of H_2/O_2 and H_2/Air AEMFCs with IrP_2-Ir_2P@NC (0.40 mg_{Ir} cm^{-2}) as the anode and commercial Pt/C (0.50 mg_{Pt} cm^{-2}) as the cathode. Operation conditions: cell temperature of 80 °C, gas back pressure of 0.2 MPa on both sides of the cell, and fully humidified H_2 and O_2 fed at a flow rate of 1000 sccm. Source data for Fig. 3 are provided as a Source Data file.

content of Ir-P bonds decreased gradually with the increase of potential (Fig. 4c, d and Supplementary Fig. 52). Additionally, it could be clearly observed that the Ir ion content of IrP_2-Ir_2P@NC was lower than that of IrP_2@NC. This indicated that an appropriate P coordination number helped promote the dissolution of Ir to form metal cations, thereby achieving a solvation enhancement effect and further improving the catalytic reaction activity, which was consistent with our hypothesis. Meanwhile, due to the enhanced solvation effect at the interface, we speculated that the dissolved Ir ions would exert a significant influence on the interfacial water (Supplementary Fig. 53).

To further observe the dynamic evolution of the Ir-P bond during the reaction, we conducted quasi-in situ XAS measurements. As shown in Fig. 4e and Supplementary Fig. 54, the Ir valence states of IrP_2-Ir_2P@NC and IrP_2@NC did not change significantly during the reaction, demonstrating that the application of voltage had no obvious effect on the electronic configuration. To further investigate the local environment of Ir atoms, we collected EXAFS spectra at the Ir K-edge under different voltages. As displayed in Fig. 4f, g, IrP_2-Ir_2P@NC and IrP_2@NC exhibited a distinct peak at 2.38 Å and 2.36 Å, respectively, which could be attributed to the Ir-P bond. With the application of voltage, without significant change in the bond length of the Ir-P bond was observed. Meanwhile, IrP_2@NC showed a persistent characteristic peak at 1.92 Å upon voltage application, which could be attributed to the Ir-O bond, indicating its excessive hydroxyl adsorption and limited desorption rate. In contrast, a distinct Ir-O bond peak in IrP_2-Ir_2P@NC was only observed at 0 V. This difference demonstrates that an appropriate amount of P coordination promotes OH transport, thereby enhancing catalytic activity in alkaline HOR. The specific structural parameters around Ir atoms were determined by curve fitting of the EXAFS spectra (Supplementary Figs. 55, 56 and Table 7). The analysis showed that with the application of voltage, the coordination numbers of the Ir-P bonds in both IrP_2-Ir_2P@NC and IrP_2@NC gradually decreased (Fig. 4h). In summary, these findings demonstrate that during the reaction, an appropriate amount of P coordination causes partial dissolution of Ir to form metal cations. This process promotes hydroxyl transport and enhances the solvation effect at the interface. Bond energy is a key parameter reflecting the stability of chemical bonds. To this end, we calculated the Ir-P bond energies in IrP_2-Ir_2P@NC and IrP_2@NC. As shown in Fig. 4i, compared with IrP_2@NC (2.34 eV), the Ir-P bond energy of IrP_2-Ir_2P@NC decreased to 1.60 eV. This further indicated that the Ir-P bonds in IrP_2-Ir_2P@NC were more prone to cleavage, generating metal cations, which thus provided

https://doi.org/10.1038/s41467-026-75394-x

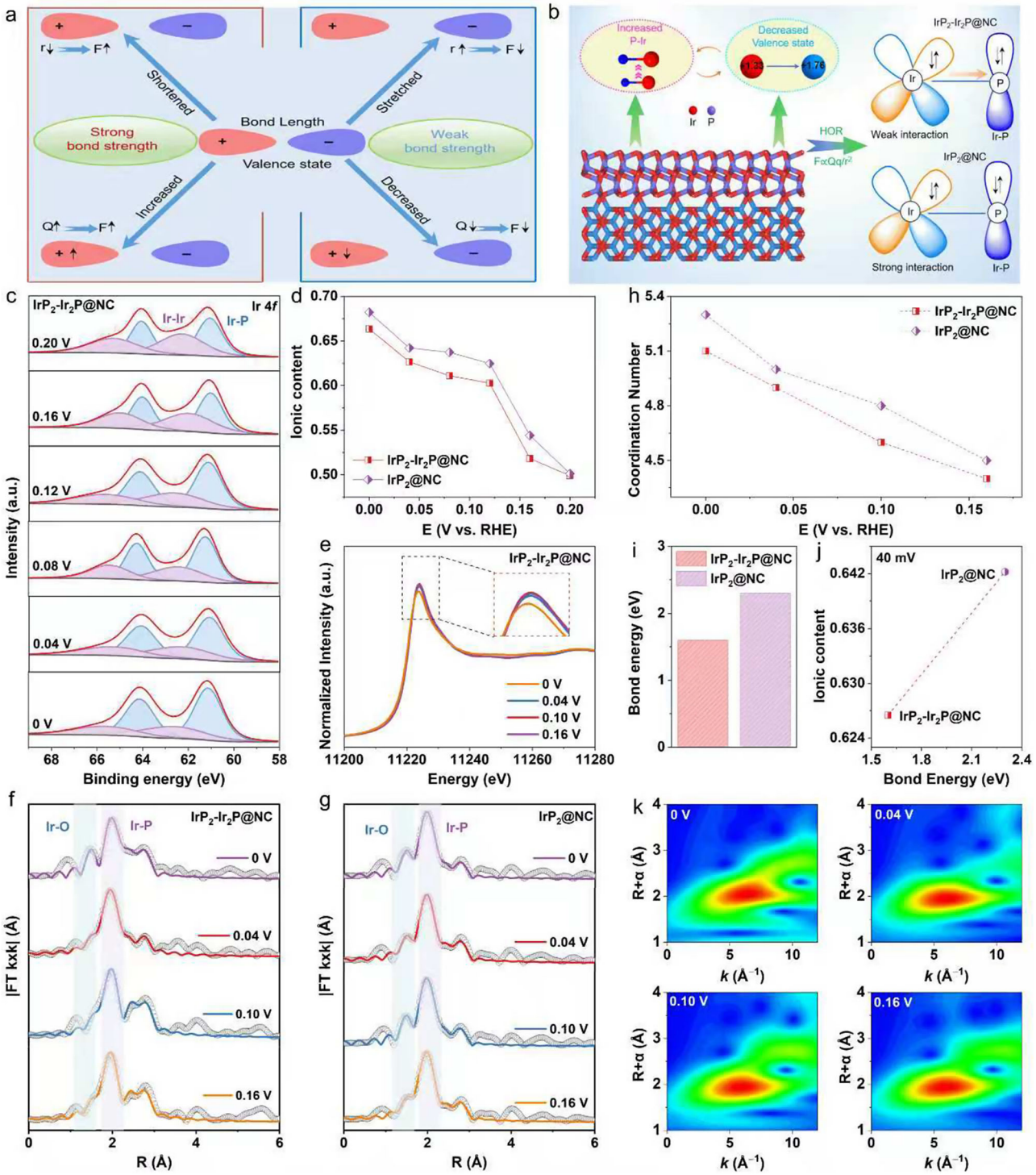

Fig. 4 | Investigation of the dynamic evolution of Ir-P bonds via quasi-in situ characterizations. a The influence of M-O bond length/valence on bond polarizability. **b** The impact of Ir-P bond length and valence state on bond strength for IrP_2-Ir_2P@NC and IrP_2@NC (red: Ir; purple: P). **c** Quasi in-situ electrochemical XPS spectra of IrP_2-Ir_2P@NC. **d** The influence of different voltages on the content of Ir ions in IrP_2-Ir_2P@NC and IrP_2@NC acquired from (c). **e** Ir L_3-edge XANES spectra of IrP_2-Ir_2P@NC at different voltages. **f** Corresponding Fourier transformed the EXAFS spectrum spectra of the IrP_2-Ir_2P@NC at different voltages. **g** Corresponding Fourier transformed the EXAFS spectrum spectra of the IrP_2@NC at different voltages. **h** The influence of different voltages on the coordination number of Ir-P bonds in IrP_2-Ir_2P@NC and IrP_2@NC The influence of different voltages on the content of Ir ions in IrP_2-Ir_2P@NC and IrP_2@NC acquired from (Supplementary Table 7). **i** Comparison of Ir-P bond energies between IrP_2-Ir_2P@NC and IrP_2@NC. **j** Relationship between Ir-P bond energy and ion content in IrP_2-Ir_2P@NC and IrP_2@NC at 40 mV acquired from (i and d). **k** Wavelet transformation of Ir L_3-edge EXAFS data for IrP_2-Ir_2P@NC at different voltages. Source data for Fig. 4 are provided as a Source Data file.

strong support for the aforementioned results (Fig. 4j). Further investigation into the different synergistic environments of IrP_2-Ir_2P@NC and IrP_2@NC showed consistency with the aforementioned EXAFS results (Fig. 4k and Supplementary Fig. 57).

P coordination-mediated Ir ion dissolution and interfacial water network regulation

In order to elucidate the impact of Ir ion dissolution (influenced by different P coordination numbers) on interfacial water, in-situ Raman spectroscopy was utilized to investigate the interfacial water structure. Isotope-labeled in-situ electrochemical Raman spectroscopy utilizing D_2O electrolyte was conducted on IrP_2-Ir_2P@NC, IrP_2@NC and Ir@NC under alkaline conditions. Figure 5a–c illustrate that spectra were obtained at different applied potentials in 0.1 M KOH, all exhibiting a broad band from 2000 to 2900 cm^{-1}, attributable to the O-H stretching vibration mode of interfacial water[49]. The O-H stretching peak of interfacial water was resolved into three distinct fractions. The O-H stretching vibration frequency at approximately 2650 cm^{-1} was ascribed to water molecules distributed in the gap region (gap-H_2O), the frequency at around 2580 cm^{-1} was linked to water molecules over the gap region (above-gap-H_2O), and the lowest O-H stretching vibration frequency at approximately 2500 cm^{-1} was associated with water molecules adjacent to the electrode surface (K·H_2O)[50]. Figure 5d depicted the potential-dependent area ratios of the peaks extracted from different catalysts, demonstrating the intensity, percentage, and variations of gap-H_2O. As expected, the proportion of gap-H_2O in IrP_2-Ir_2P@NC exceeded that in IrP_2@NC and Ir@NC, indicating the highest water concentration in the gap region. As the applied voltage grew, the proportion of gap-H_2O increased, indicating enhanced connectivity of the hydrogen-bond network in the gap-H_2O region, following the order IrP_2-Ir_2P@NC > Ir@NC > IrP_2@NC. This further suggested that the dissolution of Ir induced by an appropriate amount of P coordination augmented the number of interfacial water molecules, thereby promoting the connectivity of the hydrogen bond network.

The Stark slopes obtained by plotting the vibration frequencies as a function of electrode potential further revealed the contributions of different water components[51]. As shown in Fig. 5e and Supplementary Figs. 58, 59 compared with the Stark slopes of above-gap-H_2O and K·H_2O in IrP_2-Ir_2P@NC, IrP_2@NC and Ir@NC, the Stark slope of gap-H_2O was larger, indicating its preferential consumption during HOR. Additionally, we investigated the hydroxyl adsorption on the catalysts utilizing Zeta potential analysis. Compared with IrP_2@NC (−22.12 eV) and Ir@NC (−22.12 eV), IrP_2-Ir_2P@NC demonstrated a higher negative Zeta potential of −45.69 eV, indicating its stronger hydroxyl adsorption capacity (Fig. 5f). In summary, we concluded that moderate P coordination facilitated an increase in interfacial water content, promoting the connectivity of the hydrogen bonding network and accelerating the occurrence of HOR kinetics. Moreover, the PZC value, an important descriptor of HOR kinetics, was intimately associated with the interfacial configuration of water molecules. Figure 5g illustrates that the PZC of IrP_2-Ir_2P@NC was 0.94 eV, much lower than that of IrP_2@NC (1.14 eV) and Ir@NC (0.98 eV), correlating well with the HOR activity. Meanwhile, the enhanced hydroxyl adsorption in IrP_2-Ir_2P@NC generated a greater amount of adsorbed hydroxyl groups (OH_{ad}) and dynamically liberated more free water molecules into the gap region, thereby significantly boosting the connectivity of the hydrogen bond network (Fig. 5h). More importantly, the enhanced OH adsorption on IrP_2-Ir_2P@NC provided a greater amount of adsorbed OH_{ad} and released more free water molecules into the gap region, thereby significantly improving the connectivity of the hydrogen bond network. Figure 5i intuitively depicted the HOR catalytic mechanism of IrP_2-Ir_2P@NC, aiming to facilitate a better understanding of the reaction process.

In-situ surface-enhanced infrared absorption spectroscopy (SEIRAS) was further utilized to explore the interfacial water on the catalyst surface. Figure 6a and Supplementary Figs. 60, 61 illustrate that, in the SEIRAS spectra, the O-H stretching peak of interfacial water was decomposed into three different components. The component with the highest vibrational frequency was assigned to gap-H_2O, the intermediate frequency to above-gap-H_2O, and the lowest frequency to K·H_2O. Figure 6b presents the proportions of gap-H_2O for different catalysts at various potentials. Compared to IrP_2@NC and Ir@NC, IrP_2-Ir_2P@NC demonstrated the largest proportion of gap-H_2O, indicating its optimal hydrogen-bond network connectivity and thus competitive HOR activity. This finding was congruent with the in-situ Raman results and the HOR catalytic activity. Furthermore, as illustrated in Fig. 6c, IrP_2-Ir_2P@NC had a lesser redshift in comparison to IrP_2@NC and Ir@NC, signifying its enhancement of hydrogen bond formation, which was consistent with the above results. Supplementary Figs. 62, 63 and 64 illustrate the assessments of the electron localization function (ELF) evaluations for IrP_2-Ir_2P@NC, IrP_2@NC and Ir@NC, revealing the strongest electron interaction between IrP_2-Ir_2P@NC and adsorbed OH, succeeded by Ir@NC and subsequently IrP_2@NC[52]. This trend was consistent with the results from CO stripping cyclic voltammetry (CV) and Zeta potential measurements. Therefore, the aforementioned results demonstrated that optimal P coordination enhanced the connectedness of the hydrogen-bond network, while excessive P coordination had the contrary effect, which was consistent with the results obtained from in-situ Raman spectroscopy. To validate the theoretical effects of the interfacial water structure described above, ab initio molecular dynamics (AIMD) simulations were performed. Figure 6d–f illustrated the computed representations of regional water molecules for IrP_2-Ir_2P@NC, IrP_2@NC and Ir@NC. It could be observed that the concentration hierarchy of water molecules along the region close to the catalyst interface was detected as IrP_2-Ir_2P@NC > Ir@NC > IrP_2@NC, which was consistent with our aforementioned results. More importantly, the concentration trend reflected by these regional water molecule simulation diagrams was highly consistent with that of the oxygen density diagrams of the corresponding materials (Supplementary Figs. 65, 66 and 67). Furthermore, to investigate the impact of this alteration on the hydrogen bond network, we statistically analyzed the hydrogen bond density. As shown in Fig. 6g, h, the concentration trend of the hydrogen bond network at the interface near the catalyst was IrP_2-Ir_2P@NC > Ir@NC > IrP_2@NC, which matched the trend diagram derived from our aforementioned in-situ characterizations. In summary, these results suggested that optimal P coordination helped promote the dissolution of Ir, thereby achieving a solvation enhancement effect. This alteration enhanced the gap-H_2O content, expedited the transfer of hydroxyl species, and facilitated the connection of the hydrogen bond network, thus improving the catalytic activity of alkaline HOR. Therefore, the above results indicated that appropriate P coordination enabled IrP_2-Ir_2P@NC to achieve optimal OHBE, thereby significantly accelerating the Volmer step and realizing high catalytic activity (Fig. 6i). Furthermore, we investigated the correlations between OHBE, gap-H_2O and the catalytic performance of the catalysts at 50 mV. As shown in Fig. 6j illustrated a positive correlation among OHBE, gap-H_2O content, and catalytic activity, further indicating that an increase in gap-H_2O content was beneficial for enhancing hydroxyl adsorption and further improving the catalytic activity of HOR. In addition, we also investigated the relationship between the water formation energy barrier and the number of hydrogen bonds. As shown in Fig. 6k, the lower the water formation energy barrier, the greater the number of hydrogen bonds. Therefore, we conclude that an increase in gap-H_2O content is conducive to promoting the transport of hydroxyl species, as indicated by the Volmer step ($OH^- + H_{ad} \rightarrow H_2O + e^- + *$). This change facilitates the occurrence of the RDS, reduces the water formation energy barrier, further increases the number of hydrogen bonds, and significantly promotes the catalytic activity for the alkaline HOR. It is worth noting that the solvation enhancement effect induced by Ir dissolution mentioned above is not only applicable to the present Ir-based catalytic

https://doi.org/10.1038/s41467-026-75394-x

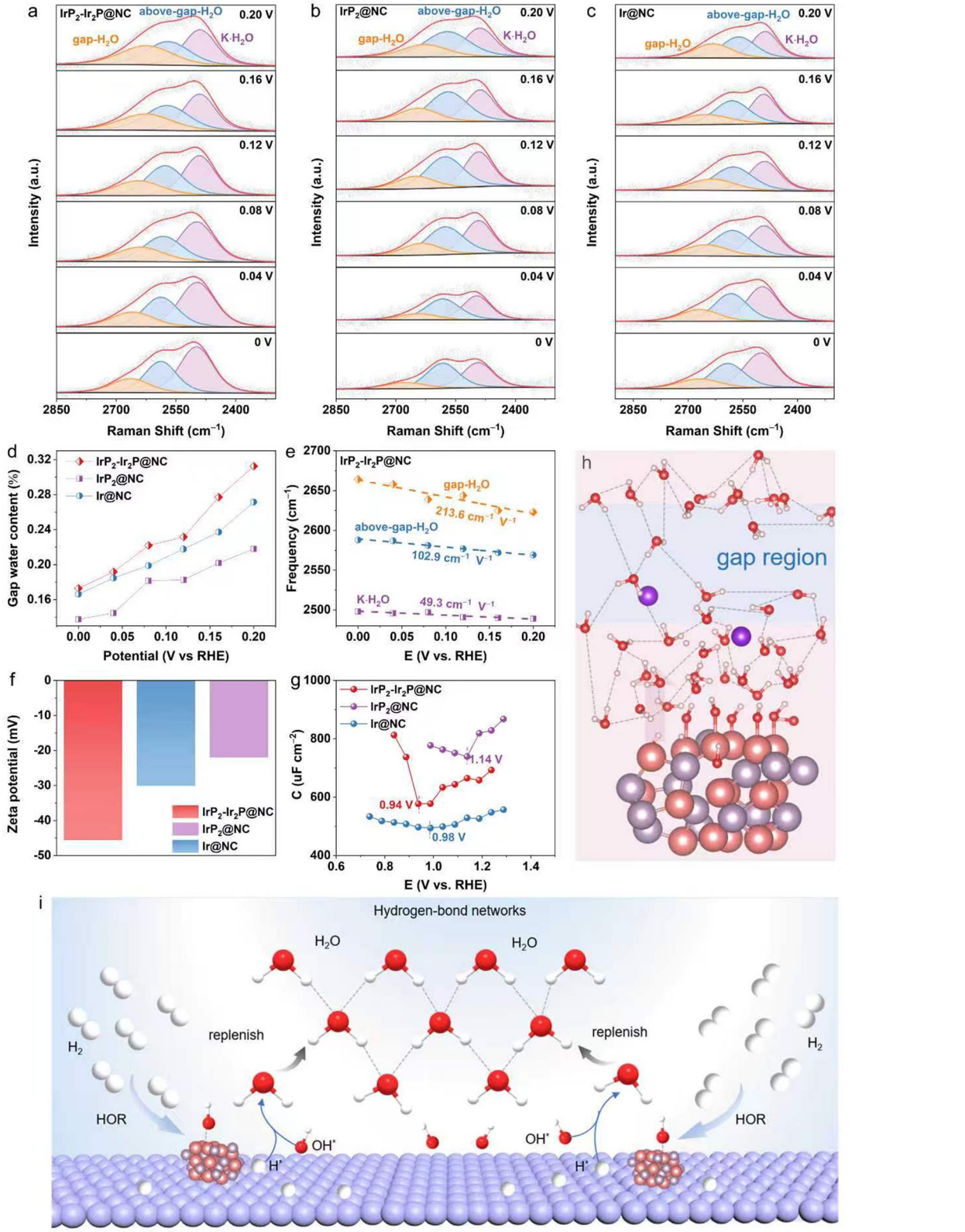

Fig. 5 | Characterization of the interfacial structures by in-situ Raman. Normalized in-situ Raman spectra of interfacial water structure on **a** IrP_2-Ir_2P@NC, **b** IrP_2@NC and **c** Ir@NC catalysts were collected. **d** The corresponding trend of the gap-H_2O content acquired from (**a**, **b** and **c**). **e** Stark slopes for IrP_2-Ir_2P@NC acquired from (**a**, **b** and **c**). **f** Zeta potential of IrP_2-Ir_2P@NC, IrP_2@NC and Ir@NC. **g** Capacity against potential curves for IrP_2-Ir_2P@NC, IrP_2@NC and Ir@NC were measured. **h** Schematic illustration of the influence of OH_{ad} on the interfacial water structure (purple: K; white: H; red: O; light purple: P; light red: Ir). **i** Schematic diagram of dynamic hydrogen bond network configuration. Dashed lines represent hydrogen bonds (white: H; red: O; light purple: P; light red: Ir). Source data for Fig. 5 are provided as a Source Data file.

https://doi.org/10.1038/s41467-026-75394-x

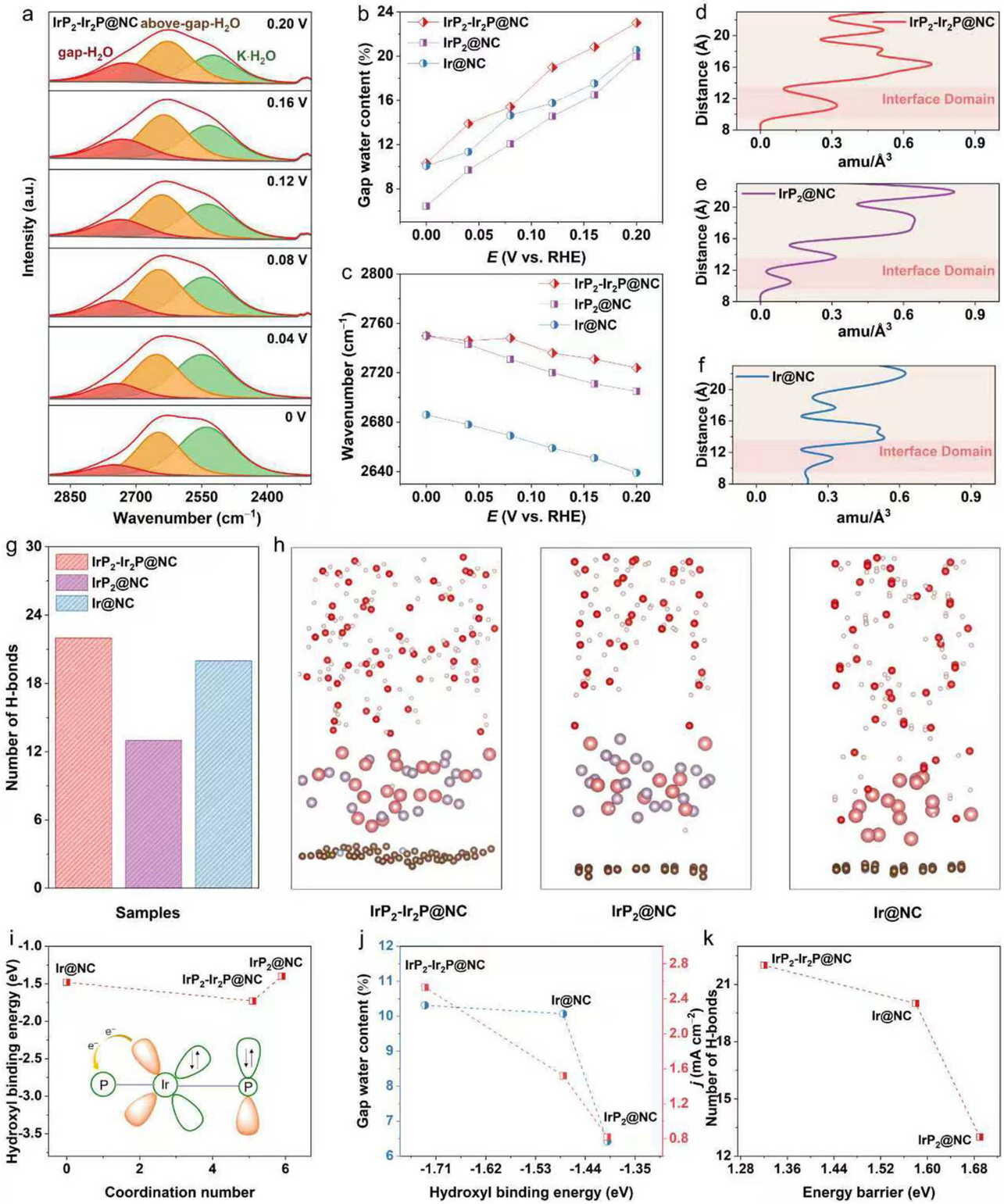

Fig. 6 | Characterization of the interfacial structures by SEIRAS and AIMD. **a** Deconvolution of the O-H stretching vibration peak from 0 V to 0.2 V vs RHE for IrP_2-Ir_2P@NC in 0.1 M KOH. **b** The corresponding trend of the gap-H_2O content acquired from (a, Supplementary Figs. 61 and 62). **c** Comparison of the O-H stretching vibration frequencies of gap-H_2O of IrP_2-Ir_2P@NC, IrP_2@NC and Ir@NC acquired from (a, Supplementary Figs. 61 and 62). **d**–**f** IrP_2-Ir_2P@NC, IrP_2@NC and Ir@NC surfaces by AIMD simulations in interfacial on the water density. **g**, **h** IrP_2-Ir_2P@NC, IrP_2@NC and Ir@NC surfaces by AIMD simulations and Average number of H-bonds in interfacial water network (gray: N; brown: C; white: H; red: O; light purple: P; light red: Ir). **i** Ir-P coordination number and OHBEs of IrP_2-Ir_2P@NC and IrP_2@NC acquired from (1 f). **j** The corresponding trends of gap-H_2O content and HOR polarization curves at 50 mV for different catalysts acquired from (1 f). **k** Variation trends of energy barriers and number of H-bonds for IrP_2-Ir_2P@NC, IrP_2@NC and Ir@NC acquired from (g and 1 h). Source data for Fig. 6 are provided as a Source Data file.

system, but also universally applicable to other noble metal-based catalysts.

Discussion

In conclusion, this work elucidates that heteroatom coordination number engineering is essential for manipulating the interfacial solvation environment and optimizing alkaline HOR performance. Theoretical simulations confirm IrP_2-Ir_2P@NC structure enables optimal H and OH adsorption to accelerate the Volmer step. A key is that tailoring Ir-based catalysts' P coordination number precisely induces controlled Ir dissolution in alkaline media, where in-situ Ir cations trigger a solvation enhancement effect (elevating gap- H_2O content and H-bond connectivity). Interestingly, we establish a universal structure-activity relationship among heteroatom coordination number, interfacial solvation state and HOR activity, clarifying the intrinsic link between metal dissolution and catalytic performance at the catalyst-electrolyte interface. More importantly, the AEMFC with IrP_2-Ir_2P@NC achieves a peak power density of 1.59 W cm^{-2} under H_2-O_2 atmosphere, and the obtained performance is competitive with data of recently reported alkaline HOR catalysts. This work departs from the conventional focus on composition/structure modulation, puts forward a design principle of "coordination number regulation → solvation effect optimization → catalytic activity enhancement", and offers fundamental insights for the rational design of electrocatalysts.

Methods

Chemicals and materials

All chemicals and solvents were commercially available and used as received without further purification. Iridium(III) chloride hydrate ($IrCl_3$, Innochem, Ir > 64%); 2-methylimidazole ($C_4H_6N_2$, 98%); Analytical grade zinc nitrate hexahydrate ($Zn(NO_3)_2{\cdot}6H_2O$, 99%); Triphenylphosphine ($C_{18}H_{15}P$, McLean, 99%), and potassium hydroxide (KOH) were sourced from Shanghai Aladdin Biochemical Technology Co., Ltd., China. Methanol was purchased from Xilong Scientific Co., Ltd. Nafion® D-521 dispersion was obtained from Alfa Aesar Chemical Co., China. Nitrogen (N_2, 99.999%) was purchased from Guilin Xinhongyi gas Co., Ltd. All experimental procedures were performed using ultrapure water with a resistivity of 18.2 MΩ cm^{-1}.

Preparation of electrolytes

To prepare 0.1 M KOH aqueous electrolyte, 5.611 g of solid potassium hydroxide was fully dissolved in ultrapure water. The resulting solution was quantitatively diluted to a final volume of 1 L volumetric flask and subsequently transferred and sealed in a polypropylene container. The electrolyte was preserved in a dry, well-ventilated environment to avoid composition degradation and performance attenuation during storage.

Synthesis of ZIF-8 and NC Precursor

To synthesize ZIF-8 precursor, 2.79 g of $Zn(NO_3)_2{\cdot}6H_2O$, 3.08 g of 2-methylimidazole were dissolved in 75 mL of methanol and sonicated for 5 min, the latter was added to the former solution and heated at 35 °C for 4 h. The resulting ZIF-8 powder was collected by centrifugation, washed several times with methanol and dried at 60 °C overnight. The ZIF-8 powders were heat-treated at 900 °C for 3 h in an N_2 atmosphere at a heating rate of 5 °C min^{-1} to obtain the final product. The black samples were collected after natural cooling to room temperature, and the final product was obtained and denoted as NC.

Synthesis of IrP_2-Ir_2P@NC, IrP_2@NC, Ir@NC

In a typical synthesis, 30 mg of previously prepared NC support, 0.066 mmol $IrCl_3$ and 0.15 mmol triphenylphosphine were slowly dissolved with 20 mL mixture solution (H_2O: ethanol = 1:1 v/v). Subsequently, the mixture solution was moved into a 100 mL Teflon-lined autoclave and heated at 160 °C for 9 h. The sample was harvested by centrifugation, washed several times with ethanol, and dried in vacuum oven overnight. The obtained sample was then annealed at 800 °C under N_2 for 2 h to get IrP_2-Ir_2P@NC.

For comparison, the fabrication of IrP_2@NC was analogous to that of IrP_2-Ir_2P@NC, except that the temperature was changed to 950 °C, as explained in the discussion section. Concurrently, Ir@NC can be synthesized without P source.

Synthesis of Ir_2P@NC

Initially, 30 mg of the as-prepared NC support, 0.066 mmol of $IrCl_3$, and 0.27 mmol of triphenylphosphine were slowly dissolved in 20 mL of a mixed solution (H_2O: ethanol = 1:1 v/v). The mixture was then transferred into a 100 mL Teflon-lined autoclave and heated at 160 °C for 9 h. The product was collected by centrifugation, washed with ethanol several times, and dried in a vacuum oven overnight. The obtained sample was subsequently annealed at 790 °C under H_2/Ar atmosphere for 2 h to obtain Ir_2P@NC.

Physical characterizations

Powder X-ray diffraction (XRD, Rigaku D/Max 2500 V/PC, Japan) was measured to investigate the crystal structure. Scanning electron microscopy (SEM) measurements were performed on the FEI Quanta 200 FEG system. Transmission electron microscopy (TEM) images were acquired on a JEM-2100F electron microscope to characterize the morphology and elemental distribution of the catalysts. Ir L_3-edge X-ray absorption spectra (XAS) were recorded at the 1W1B beamline of Shanghai Synchrotron Radiation Facility. X-ray photoelectron spectroscopy (XPS, Thermo Fisher EscaLab 250XI) was utilized to analyze the chemical state and electronic structure of the catalysts. Inductively coupled plasma mass spectrometry (ICP-MS, PerkinElmer corporation, FLexarNexION300X) was adopted to quantify the metal contents within catalyst samples. The Brunauer-Emmett-Teller (BET) method was used to measure the specific surface area and pore size distribution of the samples. Raman spectra were acquired on a Renishaw in Via spectrometer equipped with a 532 nm visible laser. Electron paramagnetic resonance (EPR) spectra were recorded with a Bruker E500 spectrometer.

Preparation of working electrodes

To prepare the catalyst inks, 3.0 mg catalysts were dispersed in 500 µL of mixed solvents containing water, isopropanol and Nafion® perfluorinated resin solution (5 wt.% in water) ($v/v/v$ = 1/1/0.02) by ultrasonication for 30 min. A glassy carbon (GC) electrode (diameter: 5 mm) was polished using slurry containing 0.05 µm γ-alumina powder, then washed sequentially with ultrapure water and ethanol to acquire a clean electrode surface. After natural air drying of the polished GC substrate, 15.0 µL of the as-prepared ink coated the electrode surface dropwise, followed by ambient air drying prior to all electrochemical tests. ICP-MS data determined the Ir mass loading deposited on the working electrode, with a final Ir loading of 47.59 μg_{Ir} cm^{-2}.

Electrochemical measurements

All electrocatalytic tests were conducted on a CHI 760E (Shanghai, China) electrochemical workstation within a standard three-electrode system. A 5 mm-diameter glassy carbon electrode (GCE, disk area: 0.196 cm^2) functioned as the working electrode, while a graphite rod and saturated KCl-filled with Ag/AgCl electrode acted as the counter and reference electrodes separately. The Biologic VMP3 multichannel potentiostat recorded electrochemical impedance spectroscopy (EIS) profiles at open-circuit potential with an upper frequency limit of 200 kHz. All electrochemical characterizations maintained a stable thermal condition of 298 (± 0.1) K, and every detected potential value converted to the reversible hydrogen electrode (RHE) scale following complete iR compensation.

Electrochemical impedance spectra (EIS) tests were conducted by the AC impedance spectra from 200 kHz to 0.1 kHz with a voltage

perturbation of 10 mV. The real part of the resistance at 1 kHz was taken as the uncompensated resistance and was used to obtain the iR-free potential (EiR-free) according to the following equation,

The Biologic VMP3 potentiostat recorded electrochemical impedance spectra (EIS) across a frequency window ranging from 200 kHz down to 0.1 kHz, applying a 10 mV alternating voltage perturbation. The resistive real component extracted at 1 kHz standed for uncompensated resistance, which further calculated iR-corrected potentials (EiR-free) via the listed formula below:

$$E_{iR-\mathrm{free}} = E - iR_{\mathrm{u}} \tag{1}$$

where E is the measured potential and i is the corresponding current.

All recorded potential values align with the reversible hydrogen electrode (RHE) scale after standard calibration procedures. Calibration proceeds in H_2-saturated electrolyte with high-purity hydrogen, where a platinum foil serves as the working electrode. Potential transformation complies with the formula listed as follows:

$$(E_{\mathrm{Ag/AgCl}} + 0.197 + 0.059 \times \mathrm{pH}) \tag{2}$$

The kinetic current density was calculated by Koutecky–Levich equation. The measured overall HOR current density (j) can be divided into kinetic current density (j_k) and diffusion current density (j_d) based on the Koutecky–Levich equation.

$$\frac{1}{j_d} + \frac{1}{j_k} = \frac{1}{j} \tag{3}$$

Where j is the measured current density, j_d is the limiting current density and j_k is the kinetic current density.

Mass activity (MA) was normalized by using j_k and the mass active metal dripped onto the RDE.

$$MA = \frac{j_k}{M} \tag{4}$$

CO stripping measurements were initially carried out in CO-saturated 0.1 M KOH solution at constant potential (0.1 V vs RHE) for 10 min to enable CO adsorption onto the metallic surface. Subsequently, the CO gas was changed to the N_2 gas and held for 30 minutes to remove the residual CO in the electrolyte. The CO stripping curve was collected by cyclic voltammetry. The CO stripping curves with different scanning rates were obtained at potential scanned from 0 V to 1.2 V vs RHE.

$$ECSA_{active\ metal} = \frac{Q_{co}}{0.42\,mC\,cm^{-2}*M} \tag{5}$$

where Q_{CO} is the total charge of adsorbed CO oxidation, 0.42 mC cm^{-2} corresponds to monolayer CO adsorption and M refers to the total loading of active metal on the working electrode.

Anion exchange membrane fuel cell (AEMFC) tests

The as-synthesized target catalyst served as the anode catalyst, and commercial Pt/C was used as the cathode catalyst. For the preparation of catalyst inks, the catalyst and alkaline ionomer dispersion (PiperION A5-HCO_3, Versogen, USA) were ultrasonically dispersed in a mixed solvent of deionized water and isopropanol. The as-prepared anode and cathode catalyst inks were separately sprayed onto two sides of the anion exchange membrane (PiperION A20-CO3, Versogen, 20 μm) to fabricate catalyst-coated membranes (CCMs). Notably, no separate independent pretreatment was performed on the pristine PiperION A20-CO3 membrane prior to catalyst spraying. Instead, full activation of the membrane was synchronously realized together with the coated catalyst layers via unified post-treatment of the entire CCM. All CCMs were immersed in 1 M KOH solution for 3 h for activation, and the fresh solution was replaced every hour. Afterwards, the CCMs were thoroughly rinsed with ultrapure water until the pH of the residual washing liquid reached neutrality. Gaskets, gas diffusion layers, graphite bipolar plates with single flow fields and metal current collectors were sequentially assembled on both sides of the treated CCM to construct a complete AEMFC single cell. The cell performance was evaluated on a Scribner 850e fuel cell test station. During the tests, both the single cell and gas humidifier were maintained at 80 °C with a relative humidity of 100%. The backpressure of H_2 was set to 200 kPa, and the backpressures of O_2 and air were both fixed at 200 kPa. In the H_2-O_2 test mode, the flow rates of H_2 and O_2 were 1.5 L min^{-1} and 1.5 L min^{-1}, respectively. In the H_2-air test mode, the flow rates of H_2 and air were both 1.5 L min^{-1}.

In-situ surface-enhanced infrared absorption spectroscopy

In-situ Fourier transform infrared (FT-IR) spectroscopy was measured using a Shimadzu IRTracer-100. For the preparation of the catalyst ink, 3 mg of the catalyst was mixed with 245 μL of isopropanol, 245 μL of ultrapure water, and 5 μL of Nafion. Then, the ink was deposited on a Si prism coated with an Au film. A platinum foil electrode and an Ag/AgCl electrode were used as the working electrode, counter electrode, and reference electrode, respectively.

In-situ Raman spectra

In-situ Raman spectra were acquired employing a customized cell (Gaoss Union), equipped with a saturated Ag/AgCl reference electrode and a carbon rod counter electrode in 0.1 M KOH. The evolution of catalyst was tracked by collecting Raman spectra at constant potential ranging from 0 to 0.20 V (vs. RHE).

DFT calculation method

All spin-polarized DFT computations were implemented via the Vienna Ab Initio Simulation Package (VASP)[53,54]. To handle exchange-correlation interactions, the Perdew-Burke-Ernzerhof (PBE) functional within the generalized gradient approximation (GGA) framework was adopted for all calculations[55]. Projector augmented-wave (PAW) pseudopotentials were utilized to characterize the electron-ion interactions in all modeled systems[56]. During structural relaxation processes, atomic configurations were fully optimized until the Hellmann-Feynman residual force acting on every single atom fell below 0.02 eV Å^{-1}. Meanwhile, the self-consistent iteration threshold for solving the Kohn-Sham equations was defined at a total energy convergence of 10^{-6} eV.

AIMD simulation details

All computational simulations were carried out within the density functional theory (DFT) formalism using the projector augmented-wave (PAW) approach encoded in the Vienna Ab Initio Simulation Package (VASP)[54,57]. The Perdew-Burke-Ernzerhof (PBE) functional belonging to the generalized gradient approximation (GGA) was chosen to describe the exchange-correlation potential[55,58]. A plane-wave kinetic energy cutoff of 400 eV was assigned for all computational sets. The self-consistent iteration convergence threshold for solving the Kohn-Sham equations was fixed at 10^{-5} eV. Full geometric relaxation was conducted for all atomic configurations until the residual Hellmann-Feynman force on each atom dropped below 0.05 eV Å^{-1}. Only the Γ-point was adopted for Brillouin zone integration throughout the simulations. Ab initio molecular dynamics (AIMD) simulations were performed under the NVT canonical ensemble with a constant temperature of 298 K, where the particle count, system volume and temperature were kept unchanged. A timestep of 2 fs(1 fs) was adopted for precise integration of atomic motion equations, and the total simulation trajectory extended up to 10 ps[59].

Data availability

The data supporting the findings of this study are available within the article and its Supplementary Information files. Source data are provided with this paper.

References

1. Jin, Y. et al. The Role of Phosphorus on Alkaline Hydrogen Oxidation Electrocatalysis for Ruthenium Phosphides. *Angew. Chem. Int. Ed.* **63**, e202406888 (2024).
2. Ren, J.-T. et al. Hydrogen Oxidation Electrocatalysts for Anion-Exchange Membrane Fuel Cells: Activity Descriptors, Stability Regulation, and Perspectives. *Energy Environ. Sci.* **17**, 3960–4009 (2024).
3. Zeng, Y. et al. Research progress of electrocatalysts for hydrogen oxidation reaction in alkaline media. *Carbon Neutral* **3**, 710–736 (2024).
4. Cai, B. et al. Unlocking Superior Hydrogen Oxidation and CO Poisoning Resistance on Pt Enabled by Tungsten Nitride-Mediated Electronic Modulation. *J. Am. Chem. Soc.* **146**, 33193–33203 (2024).
5. Cai, J. et al. Host-Guest Ensemble Effect on Dual-Pt atom-on-Rh Nanosheets Enables High-Efficiency and Anti-CO Alkaline Hydrogen Oxidation. *ACS Catal* **13**, 6974–6982 (2023).
6. Du, L. et al. Electroshock synthesis of a bifunctional nonprecious multi-element alloy for alkaline hydrogen oxidation and evolution. *Exploration* **2**, 20220024 (2022).
7. Kwofie, F. et al. Rare earth-rich sublayer tuned Pd-skin for methanol and CO tolerance oxygen reduction and hydrogen oxidation reaction. *Adv. Powder Mater.* **4**, 100305 (2025).
8. Wang, S.-Q. et al. Pd_1Ni_2 Trimer Sites Drive Efficient and Durable Hydrogen Oxidation in Alkaline Media. *J. Am. Chem. Soc.* **147**, 5398–5407 (2025).
9. Zhang, X. et al. Atomically dispersed tungsten enhances CO tolerance in electrocatalytic hydrogen oxidation by regulating the 5d-orbital electrons of platinum. *Adv. Powder Mater.* **4**, 100288 (2025).
10. Wang, Y.-H. et al. Spectroscopic Verification of Adsorbed Hydroxy Intermediates in the Bifunctional Mechanism of the Hydrogen Oxidation Reaction. *Angew. Chem. Int. Ed.* **60**, 5708–5711 (2021).
11. Strmcnik, D. et al. Improving the hydrogen oxidation reaction rate by promotion of hydroxyl adsorption. *Nat. Chem.* **5**, 300–306 (2013).
12. Stamenkovic, V. R. et al. Energy and fuels from electrochemical interfaces. *Nat. Mater.* **16**, 57–69 (2017).
13. Peng, Y. et al. Boosting alkaline hydrogen oxidation by tuning the interface of WO_3-Ir. *Rare Met* **44**, 6246–6257 (2025).
14. Meng, Z.-Y. et al. Boosting hydrogen oxidation performance of bimetallic telluride by electrochemical surface engineering. *Rare Met* **44**, 4669–4678 (2025).
15. Zhu, S. et al. The role of ruthenium in improving the kinetics of hydrogen oxidation and evolution reactions of platinum. *Nat. Catal.* **4**, 711–718 (2021).
16. Zhao, T. et al. Pseudo-Pt Monolayer for Robust Hydrogen Oxidation. *J. Am. Chem. Soc.* **145**, 4088–4097 (2023).
17. Yuan, Y. et al. Water in Electrocatalysis. *Angew. Chem. Int. Ed.* **64**, e202425590 (2025).
18. Jiang, Y. et al. Electric-Double-Layer Mechanism of Surface Oxophilicity in Regulating the Alkaline Hydrogen Electrocatalytic Kinetics. *J. Am. Chem. Soc.* **147**, 14122–14130 (2025).
19. Zhang, Y. et al. Recent Developments in Photocathodes for Solar-Driven Hydrogen Peroxide Production. *Sci. Energy Environ.* **2**, 12 (2025).
20. Ledezma-Yanez, I. et al. Interfacial water reorganization as a pH-dependent descriptor of the hydrogen evolution rate on platinum electrodes. *Nat. Energy* **2**, 17031 (2017).
21. Staszak-Jirkovský, J. et al. Water as a Promoter and Catalyst for Dioxygen Electrochemistry in Aqueous and Organic Media. *ACS Catal* **5**, 6600–6607 (2015).
22. Yang, C. et al. Bioinspired Sulfo oxygen bridges optimize interfacial water structure for enhanced hydrogen oxidation and evolution reactions. *Nat. Commun.* **16**, 6459 (2025).
23. Gao, F.-Y. et al. Nickel-molybdenum-niobium metallic glass for efficient hydrogen oxidation in hydroxide exchange membrane fuel cells. *Nat. Catal.* **5**, 993–1005 (2022).
24. Tang, C. et al. Tailoring Acidic Oxygen Reduction Selectivity on Single-Atom Catalysts via Modification of First and Second Coordination Spheres. *J. Am. Chem. Soc.* **143**, 7819–7827 (2021).
25. Wang, Y. et al. Bionic Mineralization toward Scalable MOF Films for Ampere-Level Biomass Upgrading. *J. Am. Chem. Soc.* **145**, 20624–20633 (2023).
26. Ma, X. et al. Electrochemical N_2 Conversion: Reduction and Oxidation Pathways under Mild Conditions. *Sci. Energy Environ.* **3**, 1 (2026).
27. Men, Y. et al. Boosting Alkaline Hydrogen Oxidation Kinetics through Interfacial Environments Induced Surface Migration of Adsorbed Hydroxyl. *Angew. Chem. Int. Ed.* **63**, e202411341 (2024).
28. Wu, Q. & Xu, Z. J. Mechanistic Insights into Cation Effects in Electrolytes for Electrocatalysis. *Angew. Chem. Int. Ed.* **64**, e202505022 (2025).
29. Jiao, W. et al. All-round enhancement induced by oxophilic single Ru and W atoms for alkaline hydrogen oxidation of tiny Pt nanoparticles. *Nat. Commun.* **16**, 883 (2025).
30. Cheng, H. et al. Surface Anion Promotes Pt Electrocatalysts with High CO Tolerance in Fuel-Cell Performance. *J. Am. Chem. Soc.* **144**, 22018–22025 (2022).
31. Gao, F.-Y. & Gao, M.-R. Nickel-Based Anode Catalysts for Efficient and Affordable Anion-Exchange Membrane Fuel Cells. *Acc. Chem. Res.* **56**, 1445–1457 (2023).
32. Yang, Y. et al. Unleashing efficient and CO-resilient alkaline hydrogen oxidation of Pd_3P through phosphorus vacancy defect engineering. *Chin. J. Catal.* **56**, 176–187 (2024).
33. Zeng, Y. et al. Regulating Catalytic Properties and Thermal Stability of Pt and PtCo Intermetallic Fuel-Cell Catalysts via Strong Coupling Effects between Single-Metal Site-Rich Carbon and Pt. *J. Am. Chem. Soc.* **145**, 17643–17655 (2023).
34. Lu, X. F. et al. Ultrafine Dual-Phased Carbide Nanocrystals Confined in Porous Nitrogen-Doped Carbon Dodecahedrons for Efficient Hydrogen Evolution Reaction. *Adv. Mater.* **31**, 1900699 (2019).
35. Luo, Z. et al. Spin-State Manipulation of Atomic Manganese Center by Phosphide-Support Interactions for Enhanced Oxygen Reduction. *Adv. Mater.* **37**, 2504585 (2025).
36. Huang, H. et al. Breaking Surface Atomic Monogeneity of Rh_2P Nanocatalysts by Defect-Derived Phosphorus Vacancies for Efficient Alkaline Hydrogen Oxidation. *Angew. Chem. Int. Ed.* **62**, e202315752 (2023).
37. Hong, Y. et al. Ru_2P/Ir_2P Heterostructure Promotes Hydrogen Spillover for Efficient Alkaline Hydrogen Evolution Reaction. *Adv. Energy Mater.* **14**, 2401426 (2024).
38. Wang, Q. et al. Atomic metal-non-metal catalytic pair drives efficient hydrogen oxidation catalysis in fuel cells. *Nat. Catal.* **6**, 916–926 (2023).
39. Rong, C. et al. Electronic Structure Engineering of Single-Atom Ru Sites via Co-N_4 Sites for Bifunctional pH-Universal Water Splitting. *Adv. Mater.* **34**, 2110103 (2022).
40. Yang, J. et al. Ir Nanoparticles Anchored on Metal-Organic Frameworks for Efficient Overall Water Splitting under pH-Universal Conditions. *Angew. Chem. Int. Ed.* **62**, e202302220 (2023).
41. Chen, Y. et al. Intensifying the Supported Ruthenium Metallic Bond to Boost the Interfacial Hydrogen Spillover Toward pH-Universal Hydrogen Evolution Catalysis. *Adv. Funct. Mater.* **34**, 2401452 (2024).

42. He, K. et al. Atomically Modulating Metal-Support Interactions by Isolated Co-N_4 Sites for Efficient Hydrogen Oxidation Catalysis. *Adv. Funct. Mater.* **35**, 2419609 (2025).
43. Han, Y. et al. Iridium Cluster Anchored onto Cubic Molybdenum Carbide with Strong Electronic Interactions for Robust Hydrogen Oxidation Reaction in Alkaline Medium. *Adv. Funct. Mater.* **34**, 2407060 (2024).
44. Tian, X. et al. Hydrogen Evolution and Oxidation: Mechanistic Studies and Material Advances. *Adv. Mater.* **31**, 1808066 (2019).
45. Yang, C. et al. Constructing Ordered Oxophilic Tin Sites on Platinum to Achieve a High-Performance and Anti-CO Poisoning Hydrogen Oxidation Reaction under an Alkaline Electrolyte. *ACS Catal* **15**, 869–876 (2025).
46. Luo, H. et al. Amorphous MoO_x with High Oxophilicity Interfaced with PtMo Alloy Nanoparticles Boosts Anti-CO Hydrogen Electrocatalysis. *Adv. Mater.* **35**, 2211854 (2023).
47. Zhang, X. et al. Fast and Durable Alkaline Hydrogen Oxidation Reaction at the Electron-Deficient Ruthenium-Ruthenium Oxide Interface. *Adv. Mater.* **35**, 2208821 (2023).
48. Zhang, L. et al. Emerging S-Scheme Photocatalyst. *Adv. Mater.***34**, 2107668 (2022).
49. Feng, Y. et al. Steering the Electronic Microenvironment of Ruthenium Sites via Boron Buffering Enables Enhanced Hydrogen Evolution under a Universal pH Range. *ACS Nano* **19**, 7948–7961 (2025).
50. Yue, J. et al. Hydroxyl-Binding Induced Hydrogen Bond Network Connectivity on Ru-based Catalysts for Efficient Alkaline Hydrogen Oxidation Electrocatalysis. *Angew. Chem. Int. Ed.* **64**, e202415447 (2025).
51. Li, P. et al. Hydrogen bond network connectivity in the electric double layer dominates the kinetic pH effect in hydrogen electrocatalysis on Pt. *Nat. Catal.* **5**, 900–911 (2022).
52. Scofield, M. E. et al. Role of Chemical Composition in the Enhanced Catalytic Activity of Pt-Based Alloyed Ultrathin Nanowires for the Hydrogen Oxidation Reaction under Alkaline Conditions. *ACS Catal* **6**, 3895–3908 (2016).
53. Kresse, G. & Furthmüller, J. Efficiency of ab-initio total energy calculations for metals and semiconductors using a plane-wave basis set. *Comp. Mater. Sci.* **6**, 15–50 (1996).
54. Kresse, G. & Furthmüller, J. Efficient iterative schemes for ab initio total-energy calculations using a plane-wave basis set. *Phys. Rev. B* **54**, 11169–11186 (1996).
55. Perdew, J. P. et al. Generalized Gradient Approximation Made Simple. *Phys. Rev. Lett.* **77**, 3865–3868 (1996).
56. Blöchl, P. E. Projector augmented-wave method. *Phys. Rev. B* **50**, 17953–17979 (1994).
57. Kresse, G. & Hafner, J. Ab initio molecular dynamics for open-shell transition metals. *Phys. Rev. B* **48**, 13115–13118 (1993).
58. Kohn, W. & Sham, L. J. Self-Consistent Equations Including Exchange and Correlation Effects. *Phys. Rev. A* **140**, A1133–A1138 (1965).
59. Sheng, O. et al. In Situ Construction of a LiF-Enriched Interface for Stable All-Solid-State Batteries and its Origin Revealed by Cryo-TEM. *Adv. Mater.* **32**, 2000223 (2020).

Acknowledgements

The authors gratefully acknowledge the Shanghai Advanced Research Institute, Chinese Academy of Sciences for providing characterization equipment. We also thank the State Key Laboratory of Organic-Inorganic Composites, Beijing University of Chemical Technology for the support of experimental testing facilities. Additionally, we appreciate the Key Laboratory of Functional Inorganic Material Chemistry (Heilongjiang University) and the Key Laboratory of Applied Surface and Colloid Chemistry, Ministry of Education (Shaanxi Normal University) for access to material measurement platforms and funding support.

Author contributions

B.W. and Y.Z. (Yongfa Zhu) supervised, reviewed and edited the manuscript. X.Y. provided supervision, funding acquisition and editing. C.N. and B.W. conceptualized the project, performed all the experiments, analyzed the results and wrote the original draft. Y.Z. (Yulin Zhao), Y.L., and L.C. conducted the investigation. Z.L., H.L. and T.T. curated the data. X.S., L.Z., B.W. and R.C. performed partial data testing. W.Z. and J.Q. revised the manuscript.

Funding

X.Y. discloses support for the research of this work from the National Natural Science Foundation of China [grant number 52363028, 21965005], the Natural Science Foundation of Guangxi Province [grant number 2021GXNSFAA076001, 2018GXNSFAA294077], the Guangxi Technology Base and Talent Subject [grant number GUIKE AD23023004, GUIKE AD20297039] and the Innovation Project of Guangxi Graduate Education [grant number YCBZ2024082]. W.Z. discloses support for the research of this work from the Guangdong Basic and Applied Basic Research Foundation [grant number 2025A1515010773]. B.W. discloses support for the research of this work from the National Research Foundation Singapore and A*STAR under the LCER Phase 2 Programme 1st Emerging Technology [grant number U2411D4006].

Competing interests

The authors declare no competing interests.

Additional information

Supplementary information The online version contains supplementary material available at https://doi.org/10.1038/s41467-026-75394-x.

Correspondence and requests for materials should be addressed to Xiaofeng Shi, Xiulin Yang, Yongfa Zhu or Bin Wu.

Peer review information *Nature Communications* thanks Deli Wang and the other anonymous reviewer(s) for their contribution to the peer review of this work. A peer review file is available.